Advancements in fracture toughness testing of ultra-high-strength steel sheets: Unraveling the crack-closure effect and unanticipated thickness independence

Yuya Tanaka[a, b], Naoki Hirakawa[c], Kaneaki Tsuzaki[d, b], Akinobu Shibata[d], and Hisao Matsunaga[b, e]

[a] Department of Mechanical Engineering, Fukuoka University, 8-19-1 Nanakuma, Jonan-ku, Fukuoka 814-0180, Japan

[b] Research Center for Hydrogen Industrial Use and Storage (HYDROGENIUS), Kyushu University, 744 Motooka, Nishi-ku, Fukuoka 819-0395, Japan

[c] Graduate School of Engineering, Kyushu University, 744 Motooka, Nishi-ku, Fukuoka 819-0395, Japan

[d] National Institute for Materials Science (NIMS), 1-2-1 Sengen, Tsukuba-shi, Ibaraki 305-0047, Japan

[e] Department of Mechanical Engineering, Kyushu University, 744 Motooka, Nishi-ku, Fukuoka 819-0395, Japan

[*] Corresponding author: Yuya Tanaka

E-mail: y.tanaka.vu@fukuoka-u.ac.jp

Postal Address: Department of Mechanical Engineering, Fukuoka University, 8-19-1 Nanakuma, Jonan-ku, Fukuoka 814-0180, Japan

Abstract

A novel testing method was developed to evaluate the fracture toughness of ultra-high-strength (UHS) steel sheets. The study also examined the influence of specimen thickness, utilizing specimens of varying thicknesses (1.6 ~ 10 mm). While the toughness of all specimens was determined by the threshold for planar crack propagation originating from the fatigue pre-crack-front near the mid-thickness zone, the apparent fracture toughness was dependent on specimen thickness. This phenomenon was attributed to the crack-closure effects experienced during the pre-cracking process. In-depth analyses revealed that, in the absence of crack-closure effects, the intrinsic toughness remained unaffected by changes in specimen thickness.

Keywords:

Ultra-high-strength steel; Fracture toughness; Thickness effect; Crack-closure; MT specimen

Abbreviations:

CT	compact tension
EBSD	electron backscatter diffraction
FEA	finite element analysis
IPF	inverse pole figure
IG	intergranular
IQ	image quality
MT	middle-cracked tension
OM	optical microscopy
PAG	prior austenite grain
RT	room temperature
SEM	scanning electron microscopy
SIF	stress intensity factor
UHS	ultra-high-strength

Nomenclature:

a	crack-length from the load-line
a_0	initial crack-length from the load-line
Δa	crack extension
b	uncracked ligament
b_0	initial uncracked ligament
B	specimen thickness
B_e	effective thickness

B_N	minimum thickness at the roots of the side grooves
c	length of the growing crack in the FEA model
C_0	compliance of the initial gradient line of P-V_m record
C_i	compliance of the post pop-in
E	Young's modulus
F	fraction of the flat fracture region
G_c	fracture toughness in terms of the energy release rate
G_{Ic}	resistance to the flat fracture as the work per unit area
G_{Sc}	resistance to the slant fracture as the work per unit area
HV	Vickers hardness
J_c	the toughness of instable fractures before stable tearing crack extension
J_{Ic}	resistance to the initiation of ductile cracking
J_Q	provisional toughness in terms of the J-integral
K_a	SIF for the tip of the arrested side crack
K_c	static fracture toughness
$K_{c,ap}$	apparent fracture toughness
$K_{c,eff}$	effective fracture toughness
K_g	SIF for the tip of the growing side crack
K_{Ic}	plane-strain static fracture toughness
K_{max}	the maximum SIF
K_{op}	SIF at the crack-opening point
K_Q	provisional fracture toughness
K_R	resistance to crack extension
ΔK_{eff}	effective SIF range
n	hardening exponent
P	load
P_{max}	the maximum load during the fracture toughness test
P_o	crack-opening load
P_Q	critical load to the initiation of cracking
P_y	normal load in the y-direction
r	distance from the crack-tip
R	stress ratio
R_e	residual error of V_m to $V_{m,fit}$
S	energy absorbed by plastic deformation
u	displacement in the x-direction
v	displacement in the y-direction

V_m crack-mouth opening displacement

$V_{m,fit}$ crack-mouth opening displacement without crack-closure

w displacement in the z-direction

W plate width

α yield offset

δ elongation after fracture

ε strain

ε_Y yield strain

ε_u uniform elongation

η dimensionless parameter regarding the plastic component of the J-integral

θ half-angle of the chevron notch-tip

ν Poisson's ratio

σ stress

σ_B tensile strength

σ_y normal stress in the y-direction

σ_Y yield stress

φ reduction in area

χ, ψ constants

1. Introduction

The rapid climatic changes resulting from significant emissions of greenhouse gases have led to increasingly severe natural disasters worldwide. Consequently, there is an urgent need to achieve net-zero CO_2 emissions, or carbon neutrality. Presently, all industries are actively working to reduce the CO_2 emissions associated with their operations. For example, ultra-high-strength (UHS) steel sheets with a tensile strength, σ_B, of approximately 1500 MPa have been integrated by the automobile industry into the manufacture of vehicular body parts. Such an application aims to enhance the fuel efficiency of vehicles by reducing their weight [1,2], a trend expected to encourage the adoption of higher-strength materials in various other components. In the case of thin automobile elements, it is crucial for any unstable fracture to be prevented during their service lives and, as such, static fracture toughness, K_c, is one of the most essential material properties. Since higher-strength materials typically exhibit lower K_c values as compared with lower-strength materials [3,4], the evaluation of K_c is of paramount importance for ensuring the safety of vehicles fabricated with UHS materials.

Numerous efforts have been pursued in order to understand toughness, focused primarily on the impact toughness of UHS steels from a metallurgical perspective [5–15]. For example, using quenched AISI 4340 steels with a σ_B exceeding 2000 MPa, Lai *et al.* [5] and Richie *et al.* [6, 7]

discovered that the coarse-grained materials displayed higher impact fracture toughness than those that were fine-grained. Similarly, Tomita conducted a systematic investigation to explore the effects of assorted factors on the toughness of AISI 4340 steel such as rolling ratio [8], the second phase (upper or lower bainite) included in the martensitic primal phase [9], and the contents of sulfur and calcium [10, 11]. Kimura *et al.* [12-14] demonstrated that "tempforming" — the thermomechanical processing that produces an ultra-fine elongated grain structure — also enhances the toughness of UHS low-alloy steels. Liu *et al.* [15] confirmed the excellent toughness of the steel with ultra-fine elongated grains fabricated using the deformed and partitioned process [16], with a σ_B exceeding 2000 MPa and a uniform elongation, ε_u, of more than 8%.

On the other hand, from a mechanical perspective, studies have concluded that the K_c value is affected by the thickness of a component, commonly known as the "thickness effect" [17–21]. This phenomenon is attributed to the intricate stress and strain distribution ahead of the crack-tip, extending throughout the thickness of the material. In regions of intermediate thickness, where the stress state approaches the plane strain condition, the material near the crack-tip experiences restricted deformation by the surrounding materials, resulting in high triaxiality in these zones. Consequently, the propensity for brittle fracture increases as the plastic deformation required for ductile fracture is hindered. In contrast, where the stress state approximates the plane stress condition with low stress triaxiality near the surface, the material tends to exhibit ductile fracture. Such a variation in stress state influences the fracture morphology, resulting in thickness-dependent fracture toughness for the entire crack. In general, when the component is especially thick and the plane strain condition predominates throughout, the overall resistance to cracking (*i.e.*, K_c) tends to decrease. In light of these mechanistic considerations, some research groups have proposed evaluation models to quantify the K_c value of the components with arbitrary thicknesses [22–25]. All of these models adhere to a simple energy-based concept that combines the work required to produce brittle flat fracture in the interior region and ductile slant fracture near the surface. However, it remains unclear whether any of these evaluation models are also applicable to the UHS steels, thus warranting further investigation.

As noted above, there is a major need to investigate the effect of thickness on the K_c value of UHS steels. However, only a few studies have actually addressed this issue. The primary challenge lies in the absence of a suitable evaluation method for determining the K_c of UHS steel sheets. For example, the commonly used ASTM-E399 standard [26] for assessing the fracture toughness of metallic materials focuses on evaluating the plane-strain, static fracture toughness, K_{Ic}. However, this standard was not designed to measure the K_c value of a thin sheet where a plane stress state predominates. Conversely, the ASTM-E1820 standard [27] outlines a method for measuring resistance to the initiation of ductile cracking, J_{Ic}, and the toughness of unstable fractures before stable tearing crack extension, J_c, using specimens with arbitrary thickness fabricated from ductile materials. However, its applicability to brittle UHS steels remains uncertain. Also, the ASTM-E1921 standard [28] and its similar ones [29] specify the evaluation of cleavage fracture toughness, but they are intend for ferritic steels. Additionally, although the ASTM-E561 standard [30] details the method for assessing fracture resistance in thin sheets, it primarily aims to obtain a continuous record of resistance to crack extension, K_R, plotted against crack growth. This relationship is referred to as the *K*-*R* curve and the standard lacks a procedure for determining the K_c value.

The aforementioned situation underscores the compelling need to establish an evaluation method for determining the fracture toughness of UHS steel sheets, as this is vital for ensuring the safety of the next-generation weight-saving automobiles. Consequently, our study focused on developing a novel method to measure the fracture toughness of a UHS steel with varying thicknesses.

2. Material and methods

2.1. Material

In this study, a hot-rolled, low-alloy steel plate (JIS SCM440) with a thickness of 22 mm was used, the chemical composition of which is documented in Table 1. After being maintained at 1123 K for 30 min, the plate was water-quenched, then tempered at 573 K for 60 min, followed by air cooling. This tempering condition was chosen to obtain the tensile strength over 1700 MPa. It should be noted that the thickness of the plate was halved *via* wire electro-discharge machining prior to heat treatment, *i.e.*, it was heat-treated with a thickness of about 11 mm. The mechanical properties of the material (yield stress, σ_Y; tensile strength, σ_B; yield strain, ε_Y; uniform elongation, ε_u; elongation after fracture, δ; reduction in area, φ) were obtained by tensile testing in ambient air, using a round-bar specimen with a diameter of 4 mm and a gauge length of 24 mm, at an initial strain rate of 5×10^{-5} s^{-1}. These properties are listed in Table 2, together with the data for average Vickers hardness, *HV* (load: 9.8 N; holding time: 30 s; 25-point average). Also, the nominal stress-strain diagram revealed by this tensile test is illustrated in Fig. 1. The material's initial microstructure was analyzed *via* the electron backscatter diffraction (EBSD) technique, using scanning electron microscopy (SEM) operated at an acceleration voltage of 15 kV and a beam step-size of 0.2 μm. Additionally, prior austenite grain (PAG) boundaries were observed through optical microscopy (OM) after etching treatment with the AGS etchant (produced by SANKEI Co., LTD.). The material's inverse pole figure (IPF) and image quality (IQ) maps, as well as its initial microstructure revealed after etching, are showcased in Fig. 2. The average PAG size was 13 μm, determined using the lineal intercept method in accordance with the ASTM-E112 standard [31] (inspection area: 190×190 mm; total length of the test lines: 500 mm; magnification: 178×; 5-inspection-fields average).

Table 1

Chemical composition of the material (in mass %).

C	Si	Mn	P	S	Cu	Ni	Cr	Mo	Fe
0.39	0.18	0.62	0.014	0.003	0.14	0.08	1.03	0.17	Bal.

Table 2

Mechanical properties of the material.

σ_Y [MPa]	σ_B [MPa]	ε_Y [-]	ε_u [-]	δ [%]	φ [%]	HV [-]
1470	1720	0.0074	0.0334	9.55	57.2	519

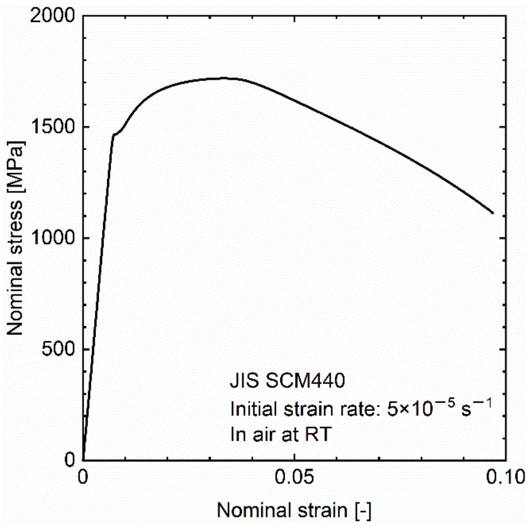

Fig. 1 Nominal stress-strain diagram of the material.

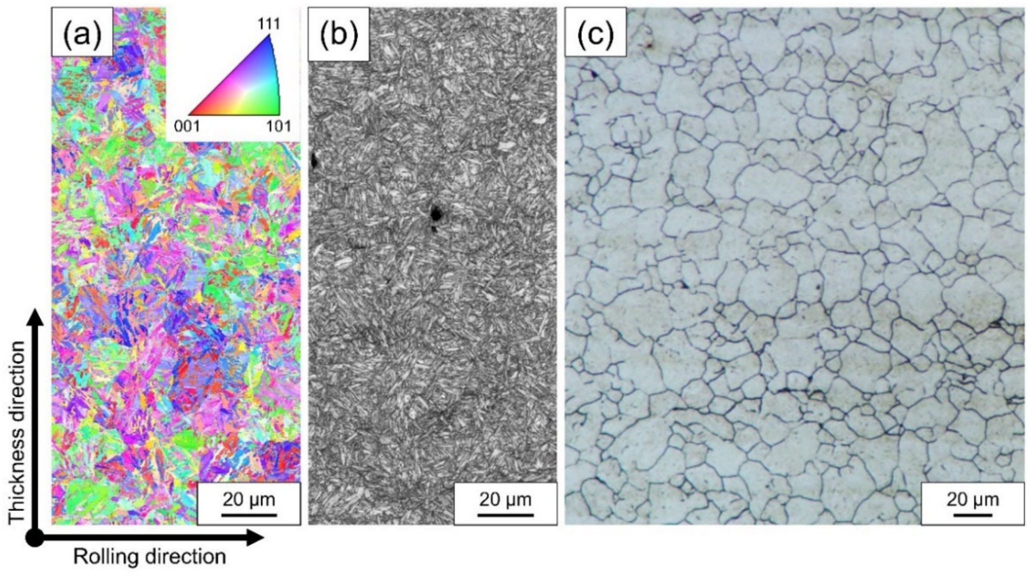

Fig. 2 Initial microstructure of the material: (a) IPF map projected normal to the inspection area; (b) IQ map; (c) OM image after etching treatment. The solid black lines in (c) correspond to the PAG boundaries.

2.2. Novel fracture toughness testing method for UHS steel sheets

As broached in Section 1, the use of the conventional fracture toughness testing methods poses many challenges for the evaluation of UHS steel sheets. The ASTM-E399 standard [26] outlines the procedure for determining the K_{Ic} value using compact tension (CT) or single edge-notched bending specimens, inappropriate for assessing the K_c value of thin materials dominated by the plane stress state. On the other hand, although the ASTM-E561 standard [30] provides guidelines for measuring the K-R curve for thin materials using middle-cracked tension (MT) specimens, it does not encompass the determination of the K_c value. While these traditional standards possess inherent strengths and weaknesses, what is noteworthy is their common measurement of the load, P, as a function of the crack-mouth opening displacement, V_m. By concentrating on this similarity, a combination of the test method outlined in ASTM-E561 and the K_{Ic} evaluation procedure specified in ASTM-E399 could potentially produce the K_c value of UHS steel sheets. Based on this hypothesis, an innovative evaluation procedure for the K_c of UHS steels is detailed herein.

2.2.1. Fracture toughness specimen suitable for a UHS steel sheet

Prior to undergoing fracture toughness testing, the specimens first needed to be pre-cracked. In the case of the MT specimens, a fatigue pre-crack was introduced from both sides of the fatigue starter-notch machined into the middle section. Ideally, the lengths of pre-cracks should be equal, but in reality, to successfully produce such a result is difficult, especially when dealing with higher-strength steels. This is due to their faster, fatigue crack-growth rates in comparison to those registered in lower-strength steels [32–34]. Schematic illustrations of two typical examples of unsuccessful cracking are exhibited in Fig. 3. In order to maintain the reliability of the test results, it is essential to achieve symmetric fatigue pre-cracking. Therefore, the effects of the specimen mounting method and the shape of the fatigue starter-notch were both investigated.

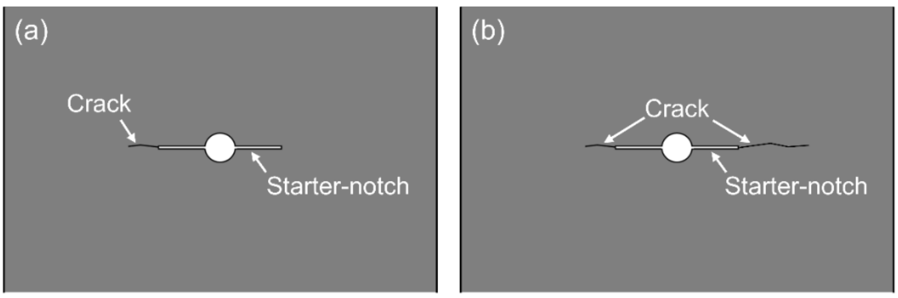

Fig. 3 Schemas of unsuccessful fatigue pre-cracking: (a) crack propagation from one side of the notch; (b) non-uniform crack propagation from both sides.

The ASTM-E561 standard [30] recommends a multiple-bolt grip or single-pin support for MT specimens. In this study, we also sought to establish which mounting method was the more appropriate for obtaining symmetrical cracking *via* elastic finite element analysis (FEA) with Abaqus 2021. The 2D, middle-cracked finite plates examined by FEA adhered to the dimensions recommended in ASTM-E561 [30] for MT specimens under tensile loading. The model simulated crack propagation from one side of two crack-tips, as reproduced in Fig. 4(a). It should be noted that the multiple-bolt grip was modeled by a fully-fixed condition (illustration on the left in Fig. 4(a)), whereas the single-pin support was modeled by a point force (illustration on the right in Fig. 4(a)). In the figure, a_0 is the initial crack-length from the load-line, c is the length of the growing crack, W is the plate-width, σ_y is the normal stress in the y-direction, and P_y is the normal load in the y-direction. In the FEA, the stress intensity factor (SIF) for the tip of the arrested side crack, K_a, and that for the tip of the growing side crack, K_g, were determined using the J-integral approach with an 8-node plane-stress element. In total, there were 1,890 ~ 2,099 nodes and 606 ~ 675 elements for the fully-fixed supported model and 2,036 ~ 2,392 nodes and 648 ~ 764 elements for the single-pin supported model. Insofar as material properties were concerned, the Young's modulus, E, of 206 GPa and the Poisson's ratio, ν, of 0.3 were adopted. In both models, the minimum mesh size was $W/600$. The FEA results are plotted against the c/W in Fig. 4(b). As featured, there is no substantial difference between the multiple-bolt grip and single-pin support below c/W = 0.07, the upper limit for fatigue pre-cracking according to ASTM-E561 [30]. The results imply that any propensity for asymmetric cracking is unaffected solely by a change in mounting method, and that other adjustments are necessary to minimize the gap between the fatigue pre-crack lengths.

Notwithstanding, specimens should be well aligned prior to loading; any bending of the specimens can negatively influence the symmetry of fatigue pre-cracking and fracture toughness testing. In this regard, the single-pin support which allows for a specimen's rotation is more advantageous than the multiple-bolt grip, since the latter can easily provoke specimen bending and misalignment. Therefore, the single-pin support method was selected for the experiments conducted in this study.

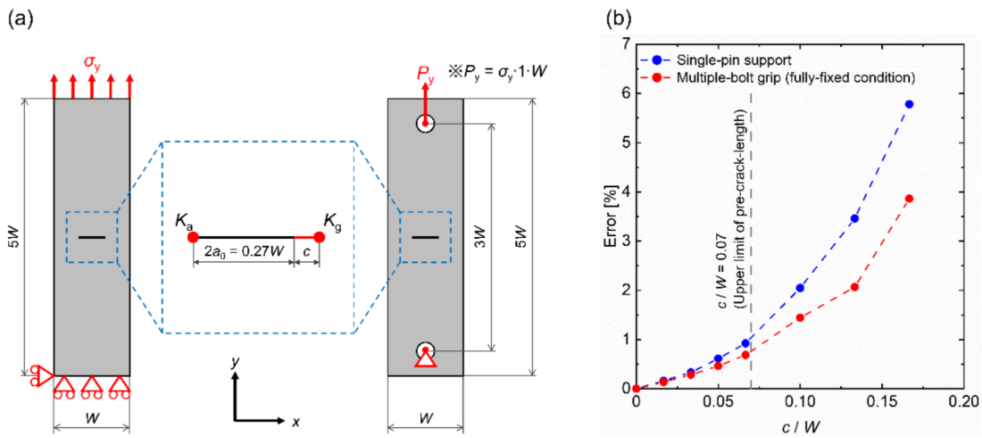

Fig. 4 Details of the FEA for consideration of specimen mounting: (a) geometry and boundary conditions for the FEA models; (b) the FEA results in both boundary conditions. The error was determined to be $(K_g - K_a)/K_a \times 100$.

According to the ASTM-E399 standard [26], three types of fatigue starter-notches are proposed (*i.e.*, a straight-through notch, a slot ending in a drilled hole and a chevron notch). Typically, the straight-through notch is preferred, while the chevron notch is recommended where the introduction of a fatigue pre-crack in a material proves difficult. As displayed in Fig. 5(a), the chevron notch-tip possesses an angle (*i.e.*, the notch-front does not cross at right angles to both sides of the specimen) and a large stress concentration is evident at the vertex. This stress concentration can equalize the crack initiation lives at both ends of the fatigue starter-notch. Two MT specimen prototypes with chevron notch-tip angles, 2θ (90° and 120°), were fabricated. The specimens were designed according to the proportion specified in ASTM E-561 [30], and the pin-hole diameter was set to $W/3$ following ASTM E-647 [35]. The crack-growth direction was oriented perpendicular to the rolling direction of the material. Fatigue pre-cracking was then carried out, the details of which will be provided in a later section. For information, the fatigue starter-notches were established *via* wire electro-discharge machining. Fig. 6 presents the successful results of fatigue pre-cracking trials. As expected, almost symmetric fatigue pre-cracks were introduced, irrespective of 2θ. The ASTM-E647 standard [35] requires that the difference between the right- and left-hand-side crack lengths in MT specimens is within $0.025W$ and that the crack lengths on the front and back surfaces do not differ by more than $0.25B$ (B is specimen thickness). The experiments conducted in this study met these requirements. Specifically, the largest bilateral gap in the pre-crack lengths was about 0.5 mm, corresponding to a c/W ratio of 0.02 in Fig. 4(b), resulting in an SIF error of less than 0.3%. Therefore, in this study, the shape of the MT specimen illustrated in Fig. 5(a) was employed.

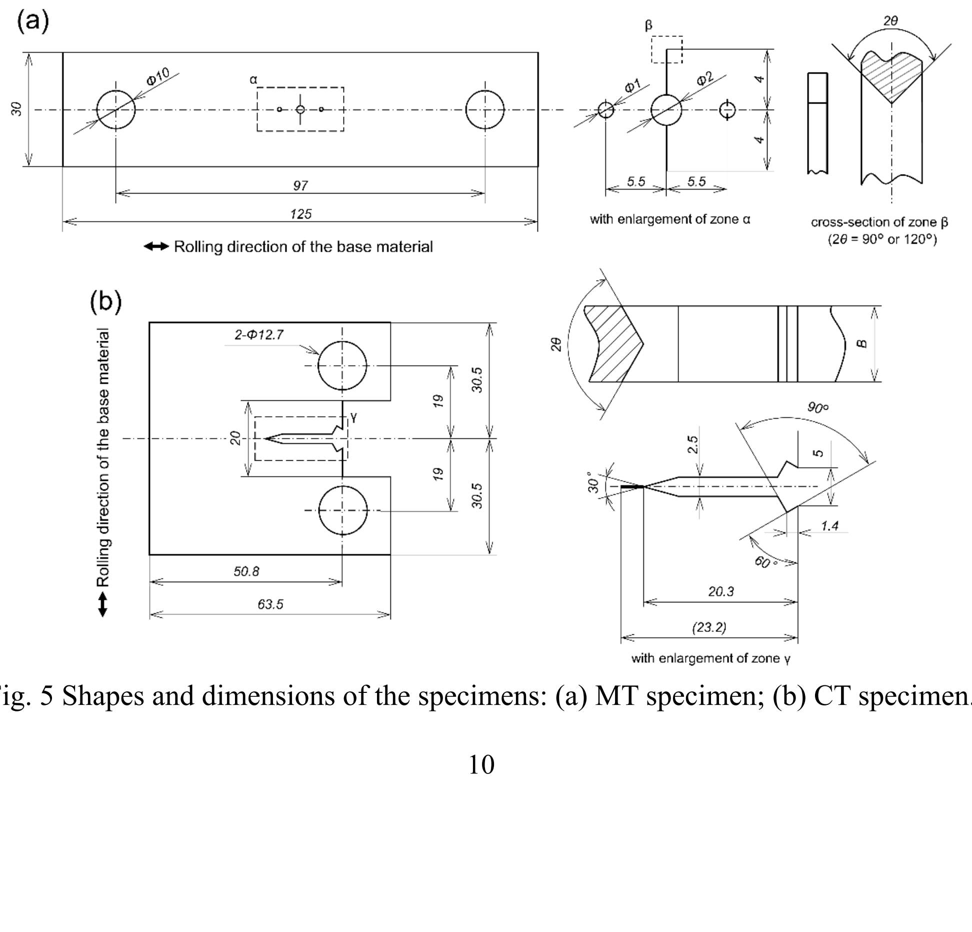

Fig. 5 Shapes and dimensions of the specimens: (a) MT specimen; (b) CT specimen.

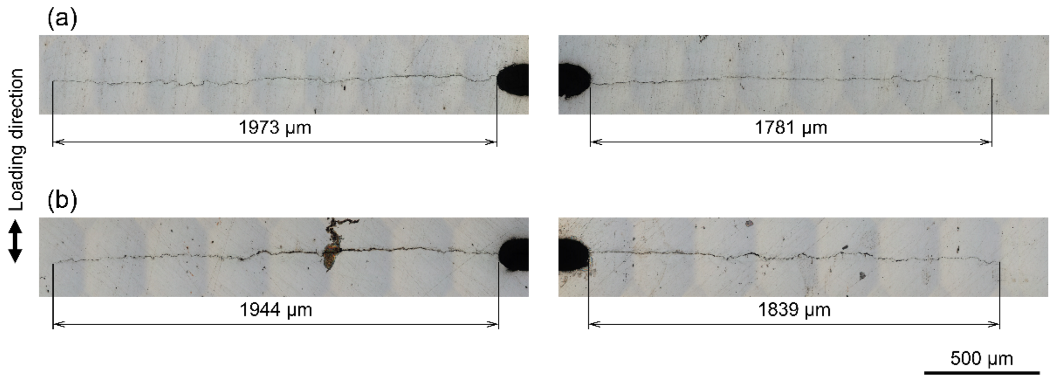

Fig. 6 OM images showing the examples of successful fatigue pre-cracking in the MT specimens: (a) $2\theta = 90°$; (b) $2\theta = 120°$.

2.2.2. *Fracture toughness testing procedure for UHS steel sheets*

The fracture toughness test of the MT specimen (specimen thickness, B: 1.6 mm) was performed using a uniaxial, servo-hydraulic, fatigue-testing machine. Monotonic tension was applied to the specimen at a constant cross-head speed that provided the initial loading rate of 0.03 MPa·m$^{1/2}$/s until final fracture. The V_m was monitored using a clip-on gauge (gauge length: 5 mm) mounted on the specimen surface by attachable knife-edges. Before the fracture toughness test, a fatigue pre-crack totaling 12 mm in length (including the starter-notch) was introduced at the stress ratio, R, of 0.1, using the aforementioned fatigue-testing machine. The constant axial loading range was periodically reduced in accordance with ASTM-E561 [30] and, at the final stage of pre-cracking, the maximum SIF, K_{max}, reached about 18 MPa·m$^{1/2}$. During tensile testing with thin specimens supported by a single pin, fractures often occur from the pin-hole, leading to invalid results. To prevent such undesirable fractures, ASTM-E338 standard [36] recommends using the reinforcing plates if the material's σ_Y is below 1380 MPa. Given that the material tested has a σ_Y of 1470 MPa, reinforcing plates were not utilized. After the fracture toughness test, the fracture surface was observed *via* OM and SEM and the value of a_0 (*i.e.*, fatigue pre-crack-length) was measured at mid-thickness and two quarter-thickness points. The average of these three measurements was taken as the value of a_0. Throughout the experiment, K was calculated using the following equation:

$$K = \frac{P}{WB}\sqrt{\pi a \cdot \sec\left(\frac{\pi a}{W}\right)} \tag{1}$$

where a is the crack-length from the load-line (including the starter-notch). In order to determine the K_c value, the critical load to the initiation of cracking, P_Q, was defined using a 5% offset secant line method in reference to ASTM-E399 [26], then the provisional fracture toughness, K_Q, was derived by applying the values of a_0 and P_Q to Eq. (1). If the ratio of the maximum load during the fracture toughness test, P_{max}, to P_Q did not exceed 1.1 *(i.e.*, $P_{max}/P_Q < 1.1$; the severest brittle criterion), with the following small-scale yielding condition fulfilled, the K_Q was regarded as K_c:

$$b > 2.5\left(\frac{K_Q}{\sigma_Y}\right)^2 \tag{2}$$

where b is the uncracked ligament when P_Q was measured. For the MT specimen, b was derived as $W/2 - a$. Additionally, the ASTM E-1820 and E-1921 standards [27,28] outline other criteria to validate whether the provisional toughness is determined by brittle cracking. In ASTM E-1820 [27], the validation based on the J-integral aspect is introduced as follows:

$$B,\ b_0 \geq 100 \times J_Q/\sigma_Y \tag{3}$$

$$\Delta a < 0.2\ \text{mm} + J_Q/(2\sigma_Y) \tag{4}$$

where Δa is crack extension, b_0 is initial uncracked ligament, and J_Q is the provisional toughness in terms of the J-integral. Taira *et al.* [37] and Hoshide *et al.* [38] proposed the following evaluation formula of J-integral value for the MT specimen:

$$J = \frac{K^2}{E} + \frac{S}{Bb} \tag{5}$$

where S is the energy absorbed by plastic deformation (the area under the P-V_m record). The precise procedure to determine the S value can be found in the reference [37,38]. In this study, J_Q was derived from Eq. (5) by substituting K_Q for K. Additionally, as discussed later, since the K_Q for the MT specimens was determined by the initiation of the crack at the middle thickness where the plane strain state is dominant (*cf.* Section 4.3), E in Eq. (5) was substituted by $E/(1-\nu^2)$. On the other hand, Δa was estimated by the iteration following ASTM-E561 [30]. The ASTM E-1921 standard [28] offers another criterion to determine the rapid propagation of V_m (pop-in) attributed to brittle fracture through the change of compliance. as follows:

$$\frac{C_i}{C_0} > \left[1 + 0.01\eta\left(\frac{W}{a_0} - 1\right)^{-1}\right] \tag{6}$$

where C_0 is the compliance of the initial gradient line of P-V_m record, C_i is the compliance of the post pop-in and η is the dimensionless parameter regarding the plastic component of the J-integral. The method to determine the value of C_i/C_0 is detailed in ASTM E-1921 [28]. Referring to Eq. (5), the η-value can be regarded as 1 for the MT specimen. In summary, the validation of K_Q was conducted following three standards (*i.e.*, ASTM E399, E-1820, and E1921). The fracture toughness test and fatigue pre-cracking for the MT specimen were conducted in ambient air at room temperature (RT).

2.3. Fracture toughness testing of CT specimens

In order to assess the effect of thickness in the present UHS steel, the K_c values in 6-mm- and 10-mm-thick materials were also measured by the fracture toughness testing of CT specimens. These tests were carried out using the same testing machine as in the experiment with the MT specimen. The CT specimens were fabricated with their crack-growth direction perpendicular to the rolling direction in the base material, the shapes and dimensions of which are detailed in Fig.

5(b). The specimens were pulled at a constant cross-head speed so that the initial loading rate was 0.03 MPa·m$^{1/2}$/s up until final fracture. The V_m during the test was recorded using a clip-on gauge attached to the machined knife-edges lying on the load-line (*cf.* Fig. 5(b)). Prior to the measurement of the K_c value, a fatigue pre-crack totaling 25.4 mm (including the starter-notch) was introduced based on the procedure specified in ASTM-E399 [26]. The K_{max} at the final stage of pre-cracking was about 15 MPa·m$^{1/2}$. Upon completion of the tests, fracture surfaces were observed *via* OM and SEM, with the values of a_0 and P_Q determined in a manner similar to that of the MT specimens (*cf.* section 2.2.2). In the CT specimen tests, K was derived using the following equations:

$$K = \frac{P}{B\sqrt{W}} \cdot f\left(\frac{a}{W}\right) \tag{7}$$

$$f\left(\frac{a}{W}\right) = \frac{2 + a/W}{(1 - a/W)^{3/2}} \cdot \left[0.886 + 4.64\left(\frac{a}{W}\right) - 13.32\left(\frac{a}{W}\right)^2 + 14.72\left(\frac{a}{W}\right)^3 - 5.6\left(\frac{a}{W}\right)^4\right] \tag{8}$$

The value of K_c was calculated in the same manner as for the MT specimen (*cf.* section 2.2.2). However, for the CT specimen, it should be noted that b in Eq. (2) is $W - a$. The J-integral value for the CT specimen can be derived using the following equation:

$$J = \frac{K^2(1 - \nu^2)}{E} + \frac{\eta S}{B b_0} \tag{9}$$

For the CT specimen, η can be determined as $2 + 0.522 b_0/W$. The J_Q value is calculated by Eq. (9). Fracture toughness testing and fatigue pre-cracking of the CT specimens were performed in ambient air at RT.

3. Results

3.1. Fracture toughness of a UHS steel sheet

Fig. 7 shows an example of the record of P against the V_m during fracture toughness testing of the MT specimens (Specimen No. 1). In this example, the K_Q value was established as 52.7 MPa·m$^{1/2}$ which could not be regarded as K_c, since it did not meet only the brittle fracture criterion following ASTM E-399 (*i.e.*, $P_{max}/P_Q > 1.1$). Table 3 summarizes the test results for the MT specimens, revealing that all tests were deemed to be invalid. On the other hand, after reaching the critical point where the experimental data crossed the 5% offset secant line, the V_m displayed rapid propagation at several points in all experiments, with a small breaking sound indicating that the crack grew intermittently in brittleness.

Fig. 8 illustrates the fracture surface of Specimen No. 1 as an example. The fracture surface can be divided into three regions (fatigue pre-cracked, flat and slant regions), as shown in Fig. 8(a). Clearly dominating the fracture surface, the flat region consisted mainly of intergranular (IG) fracture and, as characterized by SEM observation (*cf.* Fig. 8(b)), exhibited brittle fracture. In contrast, the slant region consisted of dimples, a typical feature of ductile fracture morphology (*cf.* Fig. 8(c)). These observations suggest that K_Q represents the resistance to the initiation of brittle cracking. In other words, the K_Q values for the MT specimens can be considered as valid, even though the brittle fracture criterion was unfulfilled (*i.e.*, $P_{max}/P_Q > 1.1$). Additionally, the compliance with the brittle fracture criteria specified in ASTM E-1820 and E-1921 (*i.e.*, Eqs. (3), (4), and (6)) support this hypothesis. This issue will be explored later in greater detail.

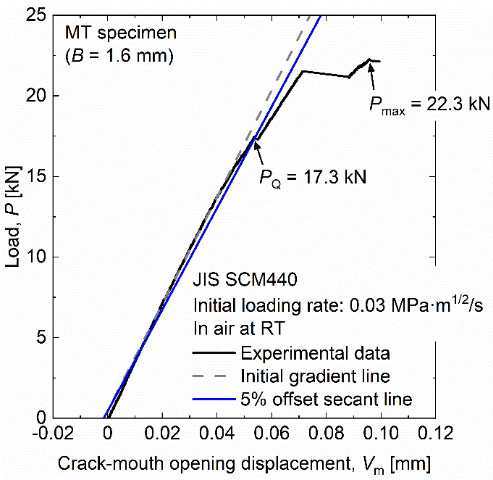

Fig. 7 An example of the P *vs.* V_m record for the MT specimen.

Table 3

Results of fracture toughness tests and validations.

Specimen No.	1	2	3	4	5	6*
Geometry		MT		CT		MT
a_0 [mm]	5.86	5.68	5.73	25.34	25.30	5.59
B [mm]		1.6		6	10	1.6
b_0 [mm]	9.15	9.32	9.27	25.47	25.53	9.40
P_Q [kN]	17.3	16.4	16.7	5.55	9.55	11.7
P_{max} [kN]	22.3	20.7	23.0	6.38	9.94	12.1
K_Q [MPa·m$^{1/2}$]	52.7	48.0	51.2	39.5	40.6	37.9
J_Q [kJ/m^2]	12.3	10.2	11.6	7.1	7.7	6.4
P_{max}/P_Q [−]	1.29	1.26	1.38	1.15	1.04	1.03
$100\times(J_Q/\sigma_Y)$ [mm]	0.83	0.69	0.79	0.48	0.52	0.43
$b-2.5\left(\frac{K_Q}{\sigma_Y}\right)^2 > 0$?	Yes	Yes	Yes	Yes	Yes	Yes
$\Delta a - \{0.2\text{ mm} + J_Q/(2\sigma_Y)\} < 0$?	Yes	Yes	Yes	Yes	Yes	Yes
$\frac{C_i}{C_0} - \left[1+0.01\eta\left(\frac{W}{a_0}-1\right)^{-1}\right] > 0$?	Yes	Yes	Yes	Yes	Yes	Yes
Decision ($K_Q = K_c$?)	No	No	No	No	Yes	Yes

*The specimen No.6 is the MT specimen with side grooves.

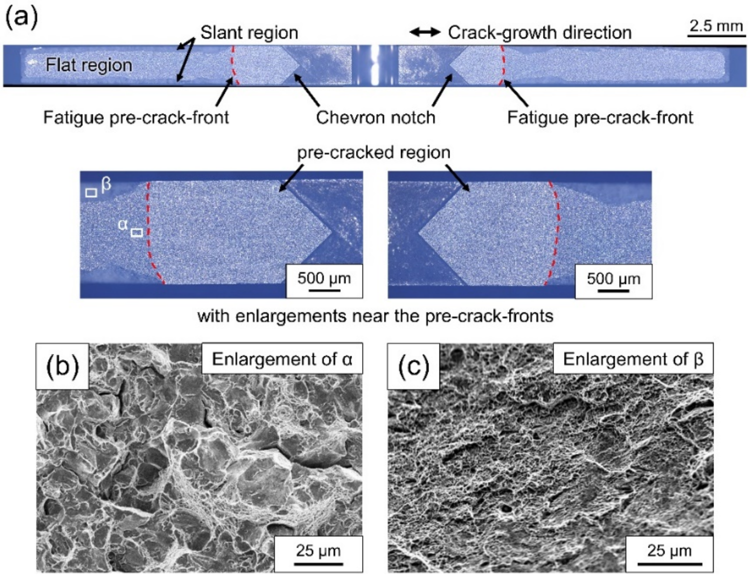

Fig. 8 Fracture surface of the MT specimen: (a) OM images; (b) and (c) SEM images corresponding to regions α and β.

3.2. Fracture toughness of CT specimens of a UHS steel

The P-V_m records of the CT specimens are featured in Fig. 9. The CT specimens also exhibited intermittent crack-growth with a breaking noise similar to the MT specimens, with all the brittle fracture criteria fulfilled only in the case of B = 10 mm (*cf.* Table 3). Regarding the fracture surfaces, there was no significant difference to be noted in either of the CT specimens. They were both almost flat and dominated by IG fracture, as can be seen in Fig. 10. Having been created by the merging of several images, some vertical stripes inadvertently appeared in Fig. 10(a) and (b). Thus, it is necessary to clarify that those streaks do not in any way derive from the surface morphologies of the CT specimens. The validity of the analysis based on the K_Q for B = 6 mm will be examined later.

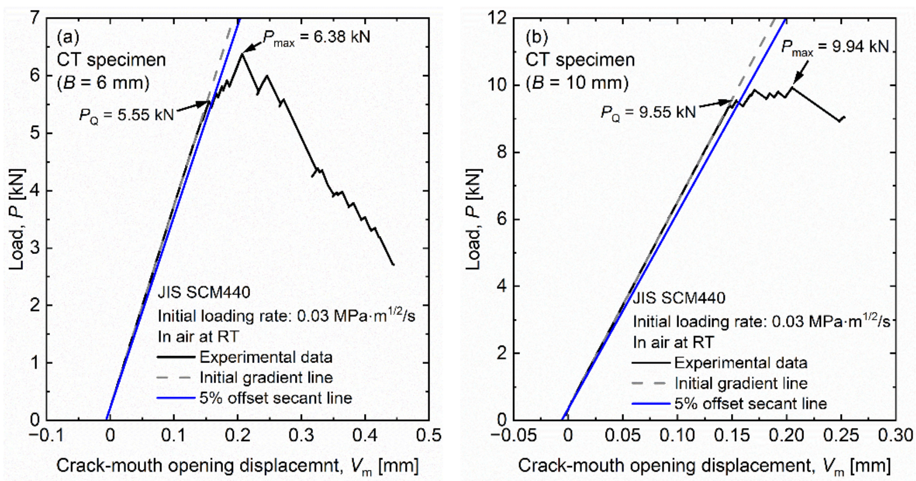

Fig. 9 The P *vs.* V_m records for the CT specimens with thicknesses of (a) 6 mm and (b) 10 mm.

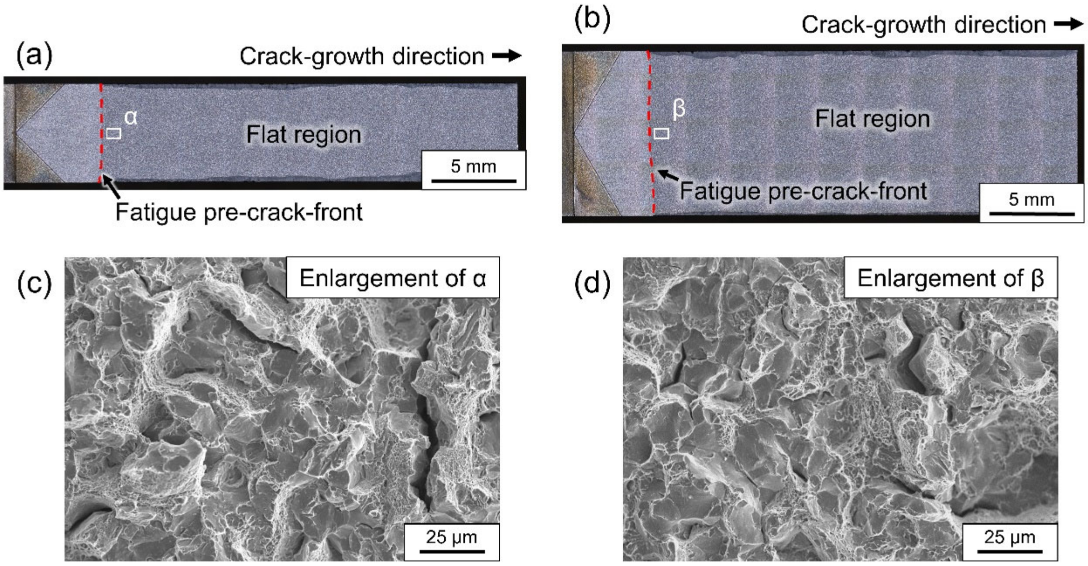

Fig. 10 Fracture surfaces of the CT specimens: (a) and (b) OM montage images of the specimens with thicknesses of 6 mm and 10 mm, respectively; (c) and (d) SEM images corresponding to regions α and β.

4. Discussion

4.1. Determination condition for the fracture toughness of UHS steel

As mentioned in Section 3.1, although the K_Q values of the MT specimens did not meet the all brittle fracture criteria, they can potentially be regarded as valid since almost all fracture surfaces featured IG fracture (*cf.* Fig. 8). In order to verify this hypothesis, a test was interrupted immediately after the first sound of a brittle break (interruption test). It must be emphasized that, barring the disruption, the test strictly followed the procedure previously described in Section 2.2.2.

The result of the interruption test (P-V_m record) is provided in Fig. 11, indicating that the test was disrupted almost at the critical point where the experimental data crossed the 5% offset secant line. After this interruption test, in order to thermally etch the fracture surface formed during tensile loading, the specimen was heat-treated at 573 K for 30 min, followed by air cooling, then fractured by tensile testing with cross-head speed of 20 mm/min in ambient air after immersion in liquefied nitrogen for 10 min. It is important to note that, before the tensile test, the specimen's ligament on the crack-plane was reduced in width *via* wire electro-discharge machining so as to facilitate easy fracture. The fracture surface obtained as a result of the interruption test is presented in Fig. 12, in which the initiated crack regions are surrounded by broken red lines. At crack initiation, only flat fracture was produced, comprised principally of IG fracture (*cf.* Fig. 12(b)). As stated in Section 1, it has been proposed in the existing literature that K_c is determined based on the following relationship [22–25]:

$$G_c = F \cdot G_{Ic} + (1 - F)G_{Sc} \tag{10}$$

where, G_c is fracture toughness in terms of the energy release rate; G_{Ic} is the resistance to flat fracture as the work per unit area; G_{Sc} is the resistance to slant fracture as the work per unit area; F is the percentage of the flat fracture region. Since the value of F is 1.0 at the crack-initiation point in the MT specimen (*cf.* Fig. 12), it is evident that K_Q is determined by the threshold for the initiation of brittle cracks, even though the brittle fracture criterion is not applicable. On the other hand, the plane stress state is generally predominant in thin components, in which the ease of ductile fracture is greater than in thick materials, as detailed in Section 1. The thickness and crack-lengths of the MT specimens were 1.6 mm and 6 mm, respectively, a combination seemingly sufficient to provoke slant fracture throughout the entire thickness of steels with σ_B lower than that of UHS steels [25,39–41]. Notwithstanding, in UHS steel, the K_c was determined to be the initiation of a brittle crack (*cf.* Fig. 12). Hence, it is more reasonable to consider that the initiation of brittle cracks dominated fracture toughness in the CT specimens. Based on the preceding discussion, all K_Q values obtained in this study were regarded as valid. Hereafter, this credible, apparent fracture toughness is denoted as $K_{c,ap}$.

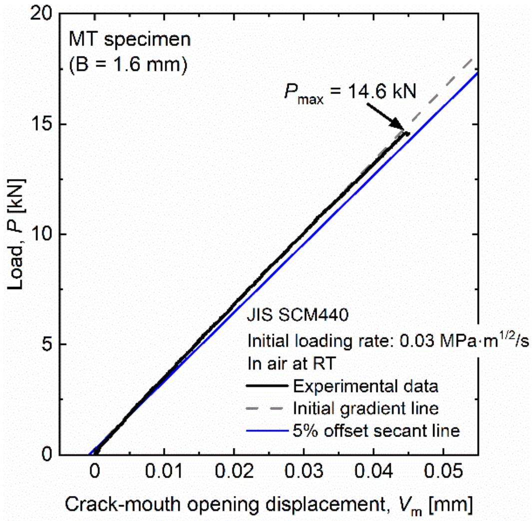

Fig. 11 The P *vs.* V_m record in the interruption test with the MT specimen. The test was halted just after crack initiation.

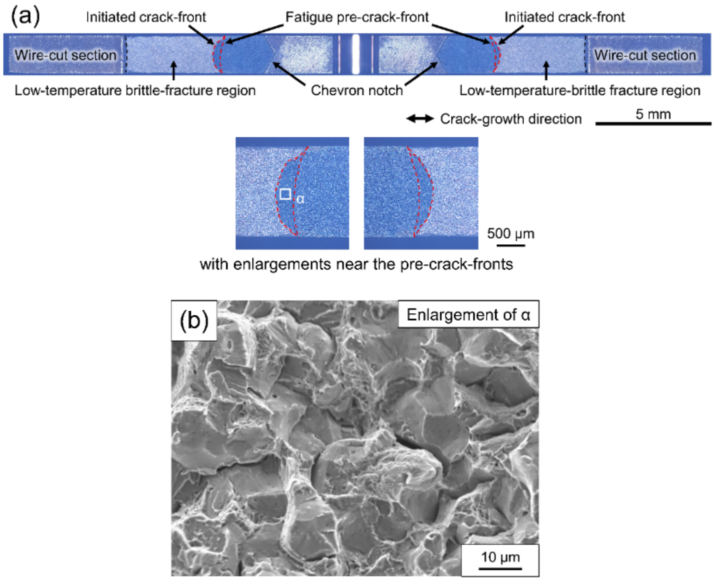

Fig. 12 Fracture surface after the interruption test: (a) OM images; (b) SEM images corresponding to region α.

4.2. *Effect of crack-closure on fracture toughness*

Based on the conventional model concerning the thickness effect on fracture toughness (*i.e.*, Eq. (10)), the K_Q of the present UHS steel with $B = 1.6 \sim 10$ mm was considered to be $K_{c,ap}$, as proposed in Section 4.1. In this scenario, this UHS steel should not exhibit the thickness dependence of $K_{c,ap}$. However, the reality was different, as depicted by the solid black circles in Fig. 13, where it is evident that the $K_{c,ap}$ of this UHS steel was clearly dependent on B. This contradiction merits the further examination which follows.

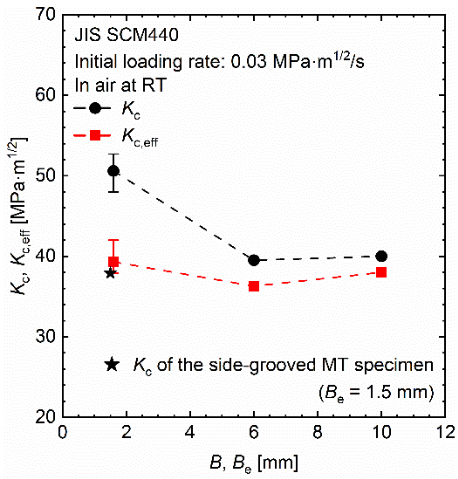

Fig. 13 Thickness dependence of fracture toughness. $K_{c,ap}$ represents apparent toughness, while $K_{c,eff}$ denotes effective fracture toughness considering crack-closure effects. For $B = 1.6$ mm, the average $K_{c,ap}$ and $K_{c,eff}$ values from three tests are displayed with error bars indicating the maximum and minimum values.

Regarding fatigue cracks, it is well known that the compressive stress field in the vicinity of a crack-tip generated by plastic deformation [42,43], as well as the roughness of a crack-face [44], the oxides wedged between the crack-wake [45], *etc.*, can hinder a crack's opening deformation. This phenomenon, known as crack-closure, reduces the effectiveness of the driving force for crack extension. The influence of crack-closure is schematically depicted in Fig. 14. During a loading process in the presence of crack-closure, a crack cannot open below a certain point. According to Elber [42,43], in a fatigue crack, the loading portion below the crack-opening load, P_o (*cf.* Fig. 14), does not contribute to crack-growth, defining the effective SIF range, ΔK_{eff}, as follows:

$$\Delta K_{eff} = K_{max} - K_{op} \tag{11}$$

where, K_{op} is the SIF at the crack-opening point. Based on this concept [46–49], considerable strides have been made and much progress recorded in the research of fatigue cracks. In this study, a similar concept for the effective crack-growth driving force was taken into account insofar as the determination of effective fracture toughness was concerned.

As stipulated in the ASTM-E399 standard, in order to minimize the impact of crack-closure on K_c, the value of K_{max} at the final stage of pre-cracking must not exceed 60% of the K_c (*i.e.*, $K_{max}/K_c < 0.6$) [26]. Even though the present fracture toughness tests satisfied this requirement ($K_{max}/K_{c,ap} \approx 0.36$ for the MT specimen and 0.38 for the CT specimen), the crack-closure introduced in the fatigue pre-cracking stage affected the test results, as shown in Fig. 15. Referring to Eq. (11), the effective fracture toughness, $K_{c,eff}$, would be derived by the following equation:

$$K_{c,eff} = K_{c,ap} - K_{op} \tag{12}$$

If the K_{op} (or P_o) is known, the $K_{c,eff}$ could be derived from this equation. The ASTM-E647 standard [35] specifies the procedure for determining the crack-opening point using unloading compliance. However, in the present study, since unloading compliance was not an option, the crack-opening point was determined according to the below-mentioned procedure, one essentially identical to the method outlined in the standard. First, the initial gradient line must be linearly approximated. Then, using this approximation, the crack-mouth opening displacement without crack-closure, $V_{m,fit}$, should be calculated as the ideal state. Next, the residual error of V_m to $V_{m,fit}$, R_e, should be evaluated *via* the following formula:

$$R_e = (V_m - V_{m,fit}) / V_{m,fit} \times 100 \tag{13}$$

Subsequently, the relationship between P and R_e can be estimated using the following equation:

$$P = \ln(R_e/\chi) / \psi \tag{14}$$

where, χ and ψ are constants. It is noteworthy to mention that Eq. (14) was determined to minimize the fitting error after a process of trial-and-error. Finally, the value of P can be derived by applying R_e = 2% to Eq. (14), with this P-value to be regarded as P_o. Here, the error margin of 2% was adopted in accordance with the recommendations of ASTM-E647 [35].

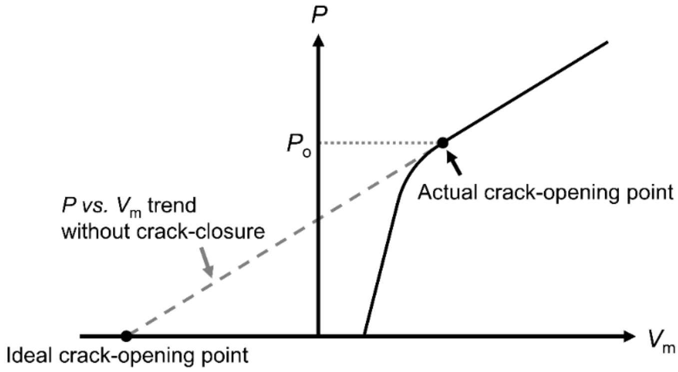

Fig. 14 Schematic illustration of the effect of crack-closure on the P *vs.* V_m trend.

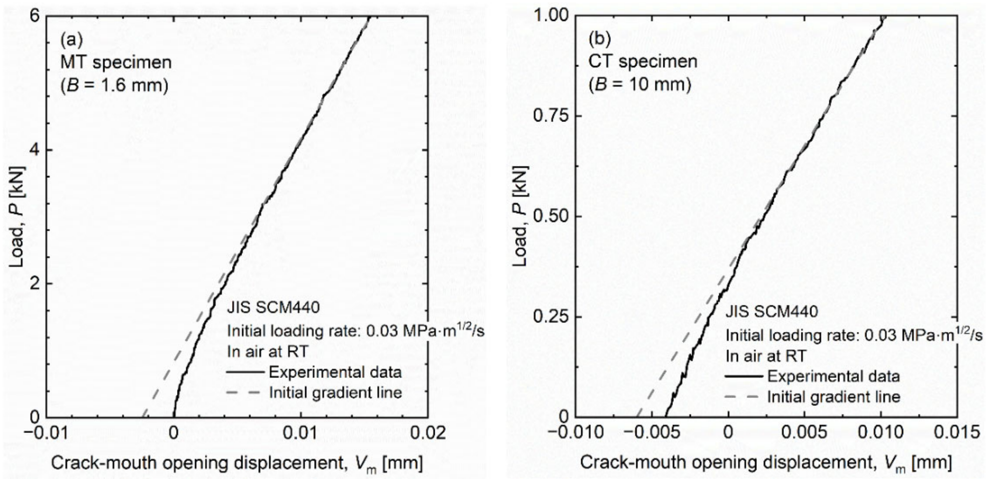

Fig. 15 Details of the P *vs.* V_m trend at the low-load regime for (a) MT and (b) CT specimens.

Fig. 16 presents the relationships between P and R_e as well as the fitting curves. The results of the determined $K_{c,eff}$ are listed in Table 4 and the $K_{c,eff}$ *vs.* B trend is also plotted in Fig. 13 using solid red rectangles. Despite the thickness effect on $K_{c,ap}$, the $K_{c,eff}$ values were almost independent of B ($K_{c,eff} \approx 40$ MPa·m$^{1/2}$). This $K_{c,eff}$ tendency aligns with the scenario proposed in Section 4.1.

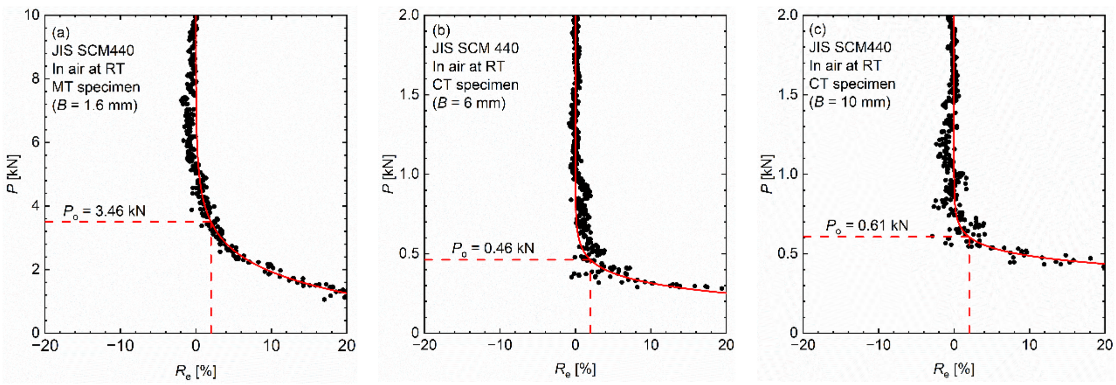

Fig. 16 Relationships between P and R_e in specimens with B = (a) 1.6 mm (Specimen No. 1), (b) 6 mm and (c) 10 mm. Fitting curves are depicted as solid red lines.

Table 4

Summary of the $K_{c,eff}$ evaluation.

Specimen No.	B [mm]	P_o [kN]	K_{op} [MPa·m$^{1/2}$]	$K_{c,ap}$ [MPa·m$^{1/2}$]	$K_{c,eff}$ [MPa·m$^{1/2}$]
1	1.6	3.46	10.7	52.7	42.0
2	1.6	3.44	10.1	48.0	37.9
3	1.6	4.26	13.1	51.2	38.1
4	6	0.46	3.2	39.5	36.3
5	10	0.61	2.6	40.6	38.0

4.3. Stress state at mid-thickness

As evoked in Section 1, the stress field in the vicinity of the crack-tip differs according to the specimen thickness. When the specimen is sufficiently thick, the plane strain state can exist in the interior region along the crack. Conversely, this stress state would disappear if the specimen thickness was ever to fall below a certain value. Furthermore, the ratio of crack-length to specimen-width, a/W, affects the plastic constraint ahead of the crack-tip [50]. Therefore, to confirm that the $K_{c,eff}$ values for each specimen thickness were determined under the equivalent fracture criterion, the stress distributions in two representative cases (MT specimen with B = 1.6 mm and CT specimen with B = 10 mm) were analyzed *via* 3D elastic-plastic FEA using Abaqus 2021. Fig. 17 showcases the 3D-FEA models and boundary conditions. The shapes and dimensions of the FEA models were the same as the actual specimens shown in Fig. 5, and the fatigue pre-crack-lengths were employed as the a values (*i.e.*, 6 mm for the MT specimen and 25.4 mm for the CT specimen). Considering the symmetry of the specimens, it is pertinent that the FEA was conducted using the one-eighth and quarter models for the MT and CT specimens, respectively. An 8-node brick element was used in these FEA, with a total of 597,883 nodes and 576,396 elements for the MT specimen and 428,310 nodes and 412,412 elements for the CT specimen. In addition, as a reference, the σ_y distribution under the plane strain condition was analyzed using a 2D elastic-plastic model. In this 2D-FEA, the CT-specimen-shaped model using a 4-node, plane strain element (9,441 nodes and 4,262 elements) was employed. In both the 3D- and 2D-FEA, the minimum mesh size was 5 µm. In all FEA, monotonic tension was applied to each model so that the SIF became 40 MPa·m$^{1/2}$ corresponding to $K_{c,eff}$ (*cf.* Section 4.2). The material's stress-strain property was approximated by the Ramberg-Osgood hardening model as follows [51]:

$$E\varepsilon = \sigma + \alpha\left(\frac{\sigma}{\sigma_Y}\right)^{n-1}\alpha \tag{15}$$

where, ε is strain, σ is stress, α is the yield offset and n is the hardening exponent. In accordance with the tensile test result (*cf.* Section 2.1), 1470 MPa for σ_Y, 0.121 for α and 17 for n were employed. Furthermore, E of 206 GPa and ν of 0.3 were adopted. Fig. 18 compares the σ_y

distributions against the distance from the crack-tip, r, at the thickness center of the MT and CT specimens, together with those in the plane strain condition. As evidenced in this figure, these distributions were virtually identical. Considering these FEA results together with the fracture morphology at the initiation stage of cracking (*cf.* Section 4.1) and the effect of crack-closure (*cf.* Section 4.2), it is concluded that the intrinsic fracture toughness, $K_{c,eff}$, of the UHS steel is identical, irrespective of B. This is the first quantitative demonstration of the thickness independence of the fracture toughness of UHS steel.

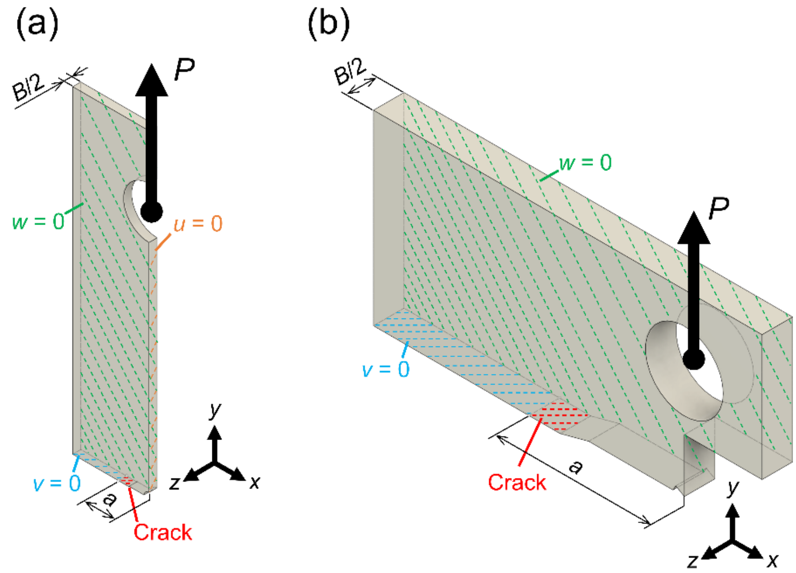

Fig. 17 Geometry and boundary conditions for the 3D-FEA models: (a) MT specimen; (b) CT specimen. The symbols u, v and w represent the displacements in the x-, y- and z-directions, respectively.

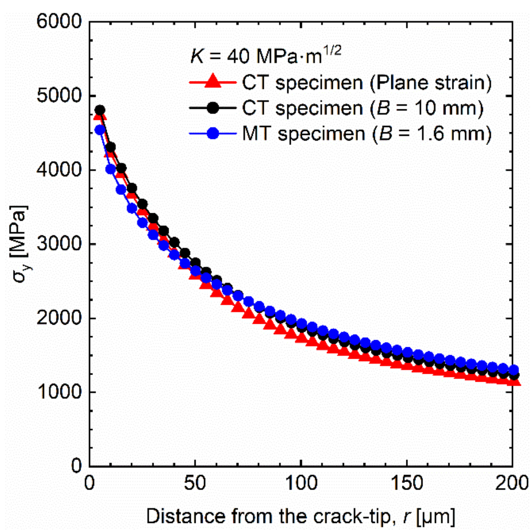

Fig. 18 Distributions of σ_y ahead of the crack-tip at the mid-thickness of the fracture toughness specimens obtained *via* FEA.

4.4. Simple evaluation of $K_{c,eff}$ using side-grooved specimen

The aforementioned results and discussions demonstrated that crack closure is responsible for the thickness dependence of the $K_{c,ap}$. As mentioned in Section 4.2, several mechanisms can evoke crack closure (*e.g.*, plasticity-induced [42,43], roughness-induced [44], and oxide-induced models [45], *etc*.). From a mechanical perspective, the plastic deformation at the near-surface, where the stress triaxiality is not so high, would dominate crack closure (*i.e.*, the plasticity-induced mechanism is dominant). In this scenario, if the plastic deformation near the surface introduced during the fatigue pre-cracking process is inhibited and/or eliminated, the value of $K_{c,ap}$ should become lower since the effective component of the applied K becomes higher. Indeed, ASTM E-399 and E-1820 standards [26,27] permit the introduction of side grooves onto the specimen surfaces to constrain plastic deformation near the surface, facilitating the measurement of K_{Ic}. By introducing side grooves after the fatigue pre-cracking process, these standards aim to obtain a straight fatigue pre-crack front by removing the lagged portion of the crack and to inhibit the plastic deformation during the fracture toughness test. However, the contribution of the side grooving in eliminating the plastic zone near the surface to reduce the crack closure is not specified. In this section, the potential for measuring $K_{c,eff}$ without the analysis discussed in Section 4.2 will be considered by conducting a fracture toughness test on an MT specimen with side grooves.

Side grooves were introduced onto both surfaces of the MT specimen with B of 1.6 mm by grinding after the fatigue pre-cracking, following the procedure described in Section 2.2.2. The depth of the side grooves was set to 0.2 mm, based on the average width of the slant region in the plane MT specimen (*cf.* Fig. 8(a)). Consequently, the minimum thickness at the roots of the side grooves, B_N, was 1.2 mm, which meets the depth requirement specified in ASTM standards (*i.e.*, $B_N/B \geq 0.75$) [26,27]. The root radius and angle were 0.08 mm and 45°, respectively. When calculating the K value for the side-grooved specimen, the evaluation formula should be corrected by substituting the effective thickness, B_e, for B. For the side-grooved MT specimen, the K value at the middle thickness can be derived with sufficient accuracy by correcting the thickness using following formula (*cf.* Appendix A):

$$B_e = B - (B - B_N)^2/B \tag{16}$$

Using this formula, the value of B_e for the present side-grooved MT specimen was determined to be 1.5 mm.

Fig. 19 shows the P-V_m record of the side-grooved MT specimen. Contrary to the plane MT specimen (*cf.* Fig. 7), the crack did not grow stably; the specimen failed after the first pop-in with only a slight increase in P. The fracture surface also differs from the plane specimen, as illustrated in Fig. 20; the slant fracture region near the surface disappeared due to the side grooves. The fracture surface was dominated by a flat fracture consisting of IG fracture, indicating that the initiation of the IG fracture determined the K_Q of the side-grooved MT specimen. The K_Q value of 37.9 MPa·m$^{1/2}$, derived from Eqs. (1) and (16), was regarded as $K_{c,ap}$ since all the brittle fracture criteria were fulfilled (*cf*. Table 3, Specimen No. 6). This $K_{c,ap}$ value almost corresponds to the average of $K_{c,eff}$ as illustrated in Fig. 13, demonstrating the advantage of introducing the side grooves after fatigue pre-cracking to eliminate the effect of crack closure on $K_{c,ap}$. Ultimately, it is concluded that the $K_{c,eff}$ of the present UHS steel can be evaluated by a simple fracture toughness test using side-grooved MT specimens. This conclusion provides an advantage in the fracture toughness assessment for commercial UHS steel sheets, where the conventional thick specimen cannot be fabricated.

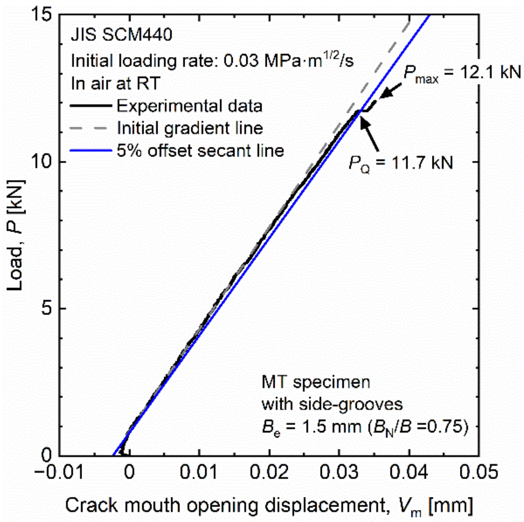

Fig. 19 The P *vs.* V_m records for the side-grooved MT specimen.

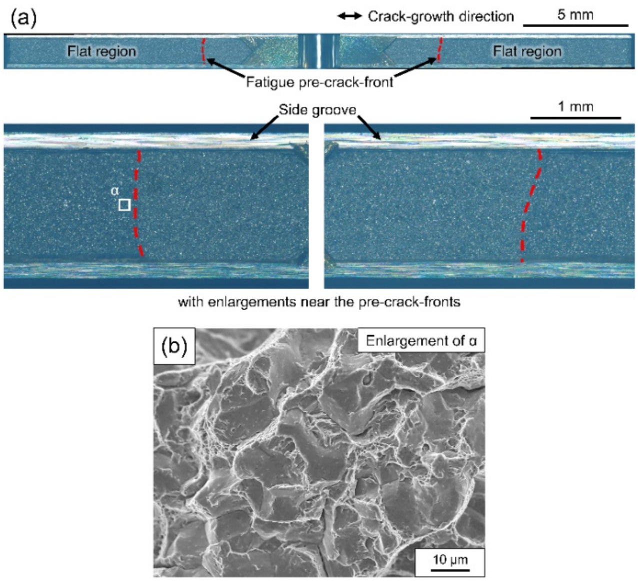

Fig. 20 Fracture surface of the side-grooved MT specimen: (a) OM images; (b) SEM images corresponding to region α.

5. Conclusions

In order to investigate the thickness effect on the apparent fracture toughness, $K_{c,ap}$, in an ultra-high-strength (UHS) steel, a specialized testing method suitable for measuring the $K_{c,ap}$ value of UHS steel was developed. Systematic fracture toughness tests were then conducted using both novel and conventional methods, covering a range of specimen thicknesses, B, from 1.6 mm to 10 mm. The main conclusions are summarized as follows:

(1) The $K_{c,ap}$ of the present UHS steel ($\sigma_B \approx 1700$ MPa) was determined by resistance to the initiation of brittle intergranular (IG) fracture, irrespective of B.

(2) Despite satisfying the fatigue pre-cracking condition ($K_{max}/K_{c,ap} < 0.6$), as stipulated by ASTM-E399, $K_{c,ap}$ was significantly influenced by crack-closure.

(3) The effective fracture toughness, $K_{c,eff}$, without the impact of crack-closure, was almost identical regardless of B. This finding indicates that the thickness effect on the $K_{c,ap}$ of UHS steel is attributed to crack-closure, highlighting the need to consider this impact during fracture toughness evaluations.

(4) The simple fracture toughness test with the side-grooved thin specimen reasonably evaluated $K_{c,ap}$ without the influence of crack closure (*i.e.*, $K_{c,eff}$). This experimental finding provides a basis for the fracture toughness evaluation of commercial UHS steel sheets using thin plate specimens.

Acknowledgments

This paper is based on results obtained from a project, JPNP 14014, commissioned by the New Energy and Industrial Technology Development Organization (NEDO), Japan. The authors would like to thank Professor Teruo Kishi (Fellow, Research Center for Advanced Science and Technology, The University of Tokyo) for his valuable comments and encouragement.

Funding: This work was partially supported by the NEDO, Japan (Grant Number: JPNP 14014) and the Iketani Science and Technology Foundation (Grant Number: 0351188-A).

Appendix A

As mentioned in Section 4.4, the evaluation formula of the SIF for side-grooved specimens should be corrected. The correction methods for the SEB and CT specimens are described in ASTM standards [26,27], but these standards do not cover the introduction of side grooves to the MT specimen. In this Appendix, the modification of the SIF evaluation for the MT specimen with side grooves is considered using elastic 3D-FEA.

Fig. A.1 showcases the 3D-FEA models and boundary conditions. The ratios of all dimensions to the crack length follow the requirement of ASTM E561 ($a/B = 5$, $2a/W = 0.4$) [30]. Considering the symmetry of the specimen, a one-eighth model, constituting the hexagonal and pentagonal elements, was used in the present FEA. The minimum mesh size was $a/1000$, and the total numbers of the nodes and elements were 22,936 ~ 155,443 and 15,800 ~ 35,700, respectively. Regarding material properties, an E of 206 GPa and a v of 0.3 were adopted. The SIF at the mid-thickness was determined using the J-integral approach under a uniform remote stress condition. Additionally, the effect of the side groove angle (*cf.* Fig. A.1) and the thickness ratio (B_N/B = 0.55 ~ 1) on the SIF were examined.

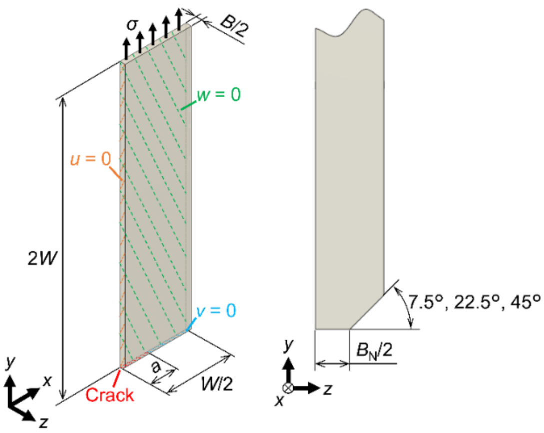

Fig. A.1 Geometry and boundary conditions for the 3D-FEA model assessing the effect of side grooves on the SIF at mid-thickness.

The correction method for the CT specimen specified in ASTM standards [26,27] is based on the analysis conducted by Shih *et al.* [52]. Their study demonstrated that the SIF of the CT specimen with side grooves can be evaluated by substituting B_e for B in Eq. (7), comparing the SIF derived from the corrected formula with that from FEA. Following their approach, the best form of the B_e providing the highest accuracy of the SIF was considered. It should be noted that the error of the SIF from the present FEA is less than 2%. Fig. A.2 showcases the present FEA results, in which K' is the SIF calculated from Eq. (1) with the substitution of various B_e values for B, and K_{FEA} is the analytical K value, demonstrating that Eq. (16) is the best formula for determining B_e in the MT specimen.

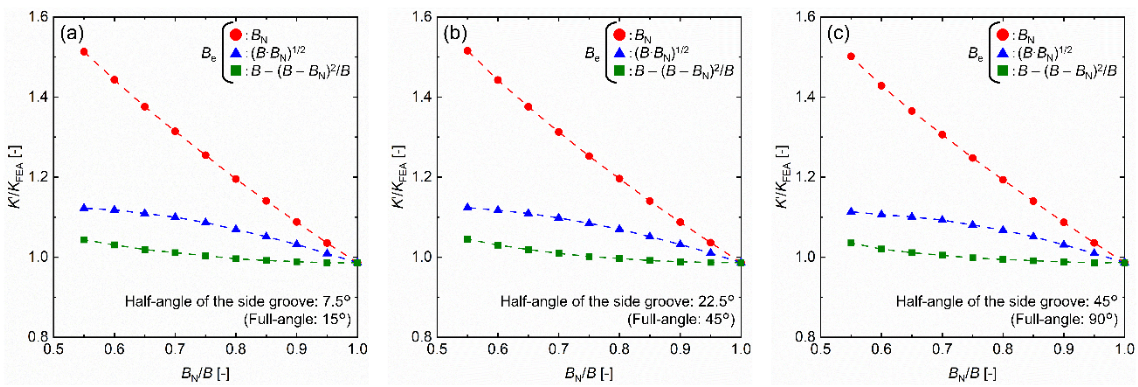

Fig. A.2 FEA results of the SIF as a function of B_N/B for the side groove's half-angle of (a) 7.5°, (b) 22.5°, and (c) 45°, respectively. The K' values were calculated with various B_e values.

References

[1] JFE Steel Corporation. JFE Steel 1.5 GPa-grade high-tensile strength cold-rolled steel sheets adopted for first time in vehicle body structural parts 2020.

[2] Unipres Corporation. Successful mass production of automotive body structural parts made of 1.5GPa ultra-high tensile steel -adopted for the first time by Nissan, incorporated into the new “Note”- 2020.

[3] Ritchie RO. The conflicts between strength and toughness. Nature Mater 2011;10:817–22. https://doi.org/10.1038/nmat3115.

[4] Kimura Y, Inoue T. Mechanical property of ultrafine elongated grain structure steel processed by warm tempforming and its application to ultra-high-strength bolt. ISIJ Int 2020;60:1108–26. https://doi.org/10.2355/isijinternational.ISIJINT-2019-726.

[5] Lai GY, Wood WE, Clark RA, Zackay VF, Parker ER. The effect of austenitizing temperature on the microstructure and mechanical properties of as-quenched 4340 steel. Metall Trans 1974;5:1663–70. https://doi.org/10.1007/BF02646340.

[6] Ritchie RO, Francis B, Server WL. Evaluation of toughness in AISI 4340 alloy steel austenitized at low and high temperatures. Metall Trans A 1976;7:831–8. https://doi.org/10.1007/BF02644080.

[7] Ritchie RO, Horn RM. Further considerations on the inconsistency in toughness evaluation of AISI 4340 steel austenitized at increasing temperatures. Metall Trans A 1978;9:331–41. https://doi.org/10.1007/BF02646382.

[8] Tomita Y. Effect of hot-rolling reduction on shape of sulfide inclusions and fracture toughness of AISI 4340 ultrahigh strength steel. Metall Trans A 1988;19:1555–61. https://doi.org/10.1007/BF02674029.

[9] Tomita Y. Effect of microstructure on plane-strain fracture toughness of AISI 4340 steel. Metall Trans A 1988;19:2513–21. https://doi.org/10.1007/BF02645479.

[10] Tomita Y. Fracture toughness of calcium-modified ultrahigh-strength 4340 steel. Metall Trans A 1990;21:2739–46. https://doi.org/10.1007/BF02646069.

[11] Tomita Y. Low fracture toughness of desulphurised 0.4C-Cr-Mo-Ni ultrahigh strength steel and its improvement. Materials Science and Technology 1991;7:97–104. https://doi.org/10.1179/mst.1991.7.2.97.

[12] Inoue T, Kimura Y, Ochiai S. Static fracture toughness of fail-safe steel. Scripta Materialia 2011;65:552–5. https://doi.org/10.1016/j.scriptamat.2011.06.025.

[13] Kimura Y, Inoue T, Tsuzaki K. Tempforming in medium-carbon low-alloy steel. Journal of Alloys and Compounds 2013;577:S538–42. https://doi.org/10.1016/j.jallcom.2011.12.123.

[14] Kimura Y, Inoue T. Influence of warm tempforming on microstructure and mechanical properties in an ultrahigh-strength medium-carbon low-alloy steel. Metall Mater Trans A

2013;44:560–76. https://doi.org/10.1007/s11661-012-1391-2.
[15] Liu L, Yu Q, Wang Z, Ell J, Huang MX, Ritchie RO. Making ultrastrong steel tough by grain-boundary delamination. Science 2020;368:1347–52. https://doi.org/10.1126/science.aba9413.
[16] He BB, Hu B, Yen HW, Cheng GJ, Wang ZK, Luo HW, et al. High dislocation density–induced large ductility in deformed and partitioned steels. Science 2017;357:1029–32. https://doi.org/10.1126/science.aan0177.
[17] Knott JF. Fundamentals of fracture mechanics. London: Butterworth; 1973.
[18] Broek D. Plane stress and transitional behaviour. Elementary engineering fracture mechanics, Dordrecht: Springer Netherlands; 1982, p. 185–218. https://doi.org/10.1007/978-94-009-4333-9_8.
[19] Gdoutos EE. Critical stress intensity factor fracture criterion. Fracture mechanics: an introduction, vol. 123, Berlin/Heidelberg: Springer-Verlag; 2005, p. 117–51. https://doi.org/10.1007/1-4020-3153-X_5.
[20] Broberg KB. Physical and engineering aspects of fracture. Cracks and Fracture, Elsevier; 1999, p. 544–623. https://doi.org/10.1016/B978-012134130-5/50009-X.
[21] Anderson TL. Fracture Mechanics: Fundamentals and Applications. CRC Press; 2017. https://doi.org/10.1201/9781315370293.
[22] Krafft JM, Sullivan AM, Boyle RW. Effect of dimensions on fast fracture instability of notched sheets. Proceedings of the Crack Propagation Symposium 1961;1:8–28.
[23] Tetelman AS, McEvily, Jr. AJ. Fracture of structural materials. New York: John Wiley & Sons, Inc; 1967.
[24] Hahn GT, Hoagland RG, Rosenfield AR, Sejnoha R. Rapid crack propagation in a high strength steel. Metall Trans 1974;5:475–82. https://doi.org/10.1007/BF02644117.
[25] Nakasa K, Takei H. The sheet thickness dependency of fracture toughness in high strength steels. ISIJ Int 1978;18:25–32. https://doi.org/10.2355/isijinternational1966.18.25.
[26] ASTM E399-20a. Standard test method for linear-elastic plane-strain fracture toughness of metallic materials 2020. https://doi.org/10.1520/E0399-20A.
[27] ASTM E1820-20b. Standard test method for measurement of fracture toughness 2020. https://doi.org/10.1520/E1820-20B.
[28] ASTM E1921-10. Standard test method for determination of reference temperature, T_o, for ferritic steels in the transition range n.d. https://doi.org/10.1520/E1921-10.
[29] Chen X, Pascual RH, Serrano M, Andres D, Nolles H, Sokolov M. Guidelines for IAEA small specimen test techniques master curve fracture toughness testing. 2020. https://doi.org/10.2172/1649107.
[30] ASTM E561-20. Standard test method for *K*-*R* curve determination 2020.

https://doi.org/10.1520/E0561-20.
[31] ASTM E112-96(2004)e2. Standard test methods for determining average grain size 2010. https://doi.org/10.1520/E0112-96R04E02.
[32] Asami K, Sugiyama Y, Terasawa M, Nasu N. Characteristics of fatigue crack growth in Cr-Mo steel (SCM 435). Journal of the Society of Materials Science, Japan 1983;32:64–70. https://doi.org/10.2472/jsms.32.64.
[33] London B, Nelson DV, Shyne JC. The effect of tempering temperature on near-threshold fatigue crack behavior in quenched and tempered 4140 steel. Metall Trans A 1988;19:2497–502. https://doi.org/10.1007/BF02645477.
[34] Sandor LT, Politori I, Gonçalves CS, Uehara AY, Leal CV, Sato M, et al. Fatigue crack propagation in nine steels, type SAE 43XX, from 0.20 to 1.00 % C, for the simulation of the fatigue behavior in a carburized layer of the SAE 4320. Procedia Engineering 2010;2:735–42. https://doi.org/10.1016/j.proeng.2010.03.079.
[35] ASTM E647-08e1. Standard test method for measurement of fatigue crack growth rates 2011. https://doi.org/10.1520/E0647-08E01.
[36] ASTM E338-03. Standard test method of sharp-notch tension testing of high-strength sheet materials n.d.
[37] Taira S, Ohtani R, Kitamura T, Yamada K. J-integral approach to crack propagation under combined creep and fatigue condition. Journal of the Society of Materials Science, Japan 1979;28:414–20. https://doi.org/10.2472/jsms.28.414.
[38] Hoshide T, Yamada A, Tanaka K. Evaluation of J integral for center-cracked plate under gross and general yieldings and its application to fatigue crack growth. Journal of the Society of Materials Science, Japan 1982;31:810–6. https://doi.org/10.2472/jsms.31.810.
[39] Shahani AR, Rastegar M, Botshekanan Dehkordi M, Moayeri Kashani H. Experimental and numerical investigation of thickness effect on ductile fracture toughness of steel alloy sheets. Engineering Fracture Mechanics 2010;77:646–59. https://doi.org/10.1016/j.engfracmech.2009.12.017.
[40] Frómeta D, Parareda S, Lara A, Molas S, Casellas D, Jonsén P, et al. Identification of fracture toughness parameters to understand the fracture resistance of advanced high strength sheet steels. Engineering Fracture Mechanics 2020;229:106949. https://doi.org/10.1016/j.engfracmech.2020.106949.
[41] Frómeta D, Cuadrado N, Rehrl J, Suppan C, Dieudonné T, Dietsch P, et al. Microstructural effects on fracture toughness of ultra-high strength dual phase sheet steels. Materials Science and Engineering: A 2021;802:140631. https://doi.org/10.1016/j.msea.2020.140631.
[42] Elber W. Fatigue crack closure under cyclic tension. Engineering Fracture Mechanics 1970;2:37–45. https://doi.org/10.1016/0013-7944(70)90028-7.

[43] Elber W. The significance of fatigue crack closure. In: Rosenfeld MS, editor. Damage Tolerance in Aircraft Structures, ASTM STP 486, American Society for Testing and Materials; 1971, p. 230–42. https://doi.org/10.1520/STP26680S.

[44] Ritchie RO, Suresh S. Some considerations on fatigue crack closure at near-threshold stress intensities due to fracture surface morphology. Metallurgical Transactions A 1982;13:937–40. https://doi.org/10.1007/BF02642409.

[45] Suresh S, Zamiski GF, Ritchie RO. Oxide-induced crack closure: an explanation for near-threshold corrosion fatigue crack growth behavior. Metallurgical and Materials Transactions A 1981;12:1435–43. https://doi.org/10.1007/BF02643688.

[46] Kikukawa M, Jono M, Tanaka K, Takatani M. Measurement of fatigue crack propagation and crack closure at low stress intensity level by unloading elastic compliance method. Journal of the Society of Materials Science, Japan 1976;25:899–903. https://doi.org/10.2472/jsms.25.899.

[47] Tanaka K, Nakai Y. Propagation and non-propagation of short fatigue cracks at a sharp notch. Fat Frac Eng Mat Struct 1983;6:315–27. https://doi.org/10.1111/j.1460-2695.1983.tb00347.x.

[48] Liaw PK, Lea TR, Logsdon WA. Near-threshold fatigue crack growth behavior in metals. Acta Metallurgica 1983;31:1581–7. https://doi.org/10.1016/0001-6160(83)90155-4.

[49] Newman J, Phillips EP, Swain MH. Fatigue-life prediction methodology using small-crack theory. International Journal of Fatigue 1999;21:109–19. https://doi.org/10.1016/S0142-1123(98)00058-9.

[50] Qingfen L, Shenghai H, Boming Z, Jiaquan W. A further study about the effect of crack depth and shape on fracture toughness. Engineering Fracture Mechanics 1991;39:219–27. https://doi.org/10.1016/0013-7944(91)90037-2.

[51] Ramberg W, Osgood W. Description of stress-strain curves by three parameters. Washington DC.: National Advisory Committee for Aeronautics (NACA); 1943.

[52] Shih CF, De Lorenzi HG, Andrews WR. Elastic compliances and stress-intensity factors for side-grooved compact specimens. Int J Fract 1977;13:544–8. https://doi.org/10.1007/BF00034260.